Periodically Time-Varying Noise Cancellation for Filtering-by-Aliasing Receiver Front Ends

Shi Bu, *Graduate Student Member, IEEE*, Sameed Hameed, *Member, IEEE*, and Sudhakar Pamarti, *Senior Member, IEEE*

***Abstract*— This article presents a periodically time-varying (PTV) noise cancellation technique for filtering-by-aliasing (FA) receivers. The key to the proposed technique is the use of a time-varying transconductance (G_m) cell to sense the noise generated by the PTV resistor in an FA receiver while maintaining the sharp filtering offered by FA. A prototype IC fabricated in a 28-nm CMOS process improves the noise figure (NF) by about 3 dB while achieving over 67-dB stopband rejection with a transition bandwidth (BW) of only four times the RF BW. A minimum in-band NF of 3.2 dB and an average in-band NF of 4.2 dB are demonstrated. With an upfront N-path filter to further enhance the linearity, the measured out-of-band IIP_3 is +18 dBm and the blocker 1-dB compression point is +9 dBm. The whole chip, including digital control circuitry, operates under a 0.9-V supply, while consuming 61-mW power at 500-MHz LO.**

***Index Terms*— Finite impulse response (FIR) filtering, noise cancellation (NC), periodically time-varying (PTV) circuit, programmable receiver, receiver front end, sampled PTV circuit, software-defined radio.**

I. Introduction

IT HAS been of significant interest in recent years to explore high-programmability surface acoustic wave (SAW)-less transceivers for emerging software-defined and cognitive radios applications [1], [2]. However, without the pre-filtering provided by SAW filters, such receivers face great challenges in simultaneously providing sufficient filtering, linearity, and low noise. Some recent approaches include N-path filters (NPFs) [3], mixer-first receivers [4], [5], and discrete-time (DT) charge-domain signal processing [6]. They have demonstrated moderate filtering (usually equivalent to first- or second-order baseband filters), reasonably high small- and large-signal linearity [approximately +20-dBm out-of-band (OOB) IIP_3 and +10-dBm blocker 1-dB compression point (B_{1dB})], good noise performance, and moderate LO and bandwidth (BW) tunability.

Manuscript received February 29, 2020; revised July 24, 2020 and August 28, 2020; accepted September 27, 2020. Date of publication October 19, 2020; date of current version February 24, 2021. This paper was approved by Associate Editor Alyosha Molnar. This work was supported in part by the National Science Foundation under Award ECCS 1408647 and Award ECCS 1810268, and in part by the Broadcom Foundation Fellowship Program. *(Corresponding author: Shi Bu.)*

Shi Bu and Sudhakar Pamarti are with the Department of Electrical and Computer Engineering, University of California, Los Angeles, CA 90095 USA (e-mail: shibu@ucla.edu).

Sameed Hameed is with Silvus Technologies, Inc., Los Angeles, CA 90024 USA.

Color versions of one or more of the figures in this article are available online at https://ieeexplore.ieee.org.

Digital Object Identifier 10.1109/JSSC.2020.3028357

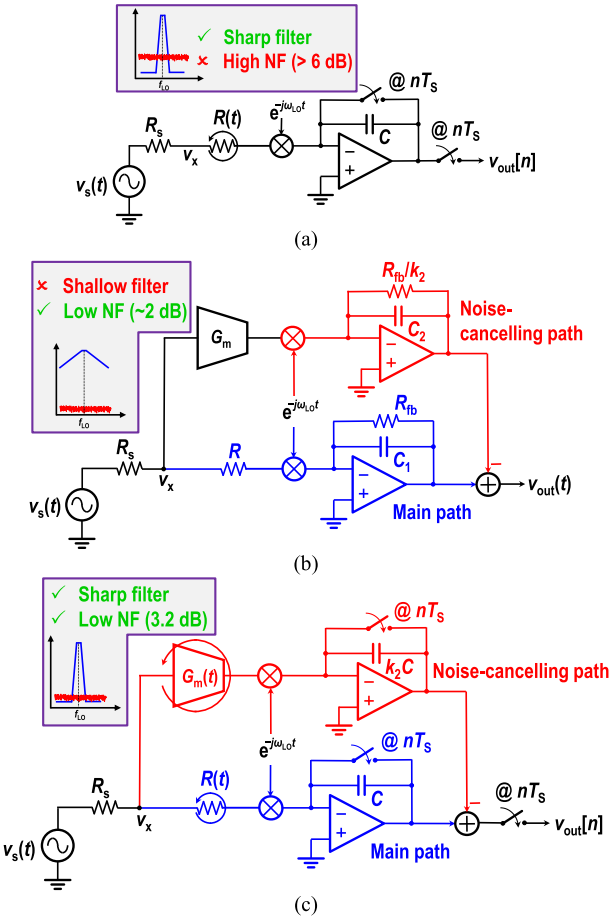

Fig. 1. (a) FA receiver using a PTV resistor for sharp filtering [9]. (b) NC for mixer-first receiver using an LTI G_m cell at RF [5]. (c) Proposed PTV NC for FA receiver to achieve both sharp filtering and low noise.

On the other hand, the recent filtering-by-aliasing (FA) technique [7]–[10] provides very sharp analog finite impulse response (FIR) filtering (>70-dB rejection at 4 × RF BW[1] offset), good linearity (> +20-dBm OOB IIP_3 and +13-dBm B_{1dB}), and comparable or better programmability. The block diagram of a representative active FA receiver is shown in Fig. 1(a), wherein the key component is an input matching resistor that is periodically time-varying (PTV), $R(t) = R(t + T_s)$. Together with a mixer and the baseband integrate-and-dump circuit, equivalently the input signal $V_s(t)$ is downconverted to baseband and sees an apparent

[1]RF BW is twice the baseband bandwidth.

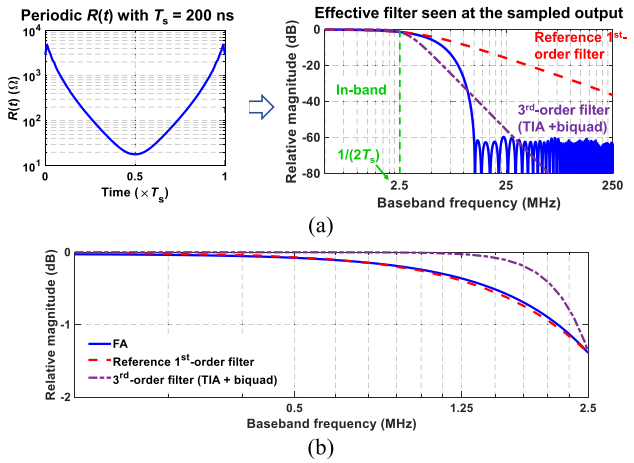

Fig. 2. (a) Example of $R(t)$ variation and the corresponding normalized baseband filter. (b) Zoomed-in view showing the filter droop in the passband.

linear time-invariant (LTI) filter at the sampled output, whose impulse response is given by [9]

$$g(\tau) = \frac{1}{C[R_s + R(-\tau)]} \tag{1}$$

where $0 \le \tau \le T_s$. The FA receiver presents a time-varying impedance to the antenna with an S_{11} given by

$$S_{11} = \text{mean}\left[\frac{R(t) - R_s}{R(t) + R_s}\right] \tag{2}$$

where R_s is the antenna impedance (typically 50 Ω). Although the desire for a small S_{11} (typically –10 dB or less) constrains the choice of $R(t)$, fairly arbitrary impulse response shape, $g(\tau)$, and, hence, very sharp analog FIR filtering can be achieved by choosing $R(t)$ appropriately. An example of the $R(t)$ variation and the corresponding baseband filter is shown in Fig. 2, which shows that FA is much sharper than a first-order filter. A third-order baseband filter equivalent resulting from a TIA plus biquad combination that is commonly used in traditional mixer-first and N-path designs is also shown for the sake of comparison. Note that the in-band droop, filter transition BW, and stopband attenuation of the FA filter can be traded against each other. Furthermore, sharper filtering was reported using time interleaving (TI) that also relaxes the S_{11} constraint [10], making it extremely useful for software-defined radio applications. In any case, the overall receiver's noise is fundamentally limited by the noise contribution from $R(t)$. In fact, during part of each period, its value can get very large ($>10\times$ the 50-Ω antenna resistance), resulting in an overall high noise figure (NF) of >6 dB after considering the NF degradation due to LO harmonics and filter aliasing [9], [10]. This disadvantage prohibits it from being used in more generic RF environments where a low NF may be desired.

On the other hand, noise cancellation (NC) technique has been proven useful to lower the NF of wideband low-noise amplifiers (LNAs) [11]. The frequency-translational NC (FTNC) technique has been successfully extended to mixer-first receivers to cancel the noise contribution of their input matching resistor, and an NF as low as 2 dB was demonstrated in [5]. As shown in Fig. 1(b), generic LTI-NC senses the noise voltage from the input matching resistor at the RF node, V_x, with a transconductance (G_m) cell and cancels this noise by subtracting the signals at the outputs of the main and NC paths, where a baseband gain factor k_2 is used to control the relative gain between the two paths. In principle, such FTNC can be readily extended to FA receivers as well. However, as will be shown in Section II, such naïve NC will lower the NF of an FA receiver, but it will negate the sharp filtering of FA.

In [12], a PTV-NC technique tailored for the FA-based receivers was proposed, which improves the average in-band NF ($NF_{avg,IB}$) by about 3 dB and achieves a minimum in-band NF ($NF_{min,IB}$) of 3.2 dB without noticeable degradation to FA filtering performance, shown in Fig. 1(c). This article details the design of the PTV-NC in [12] together with supporting theoretical analysis on both filtering and noise. In addition, upfront N-path filtering is added to improve the linearity of the front end [12]. To the authors' best knowledge, this is the first application of a combination of an upfront NPF and an FA receiver. The attendant design considerations are also presented in this article. Section II details how the naïve application of LTI-NC to FA receivers is not useful and then introduces the proposed PTV-NC technique. Section III explains the dynamic range (DR) and linearity issue faced by the proposed technique and describes how an upfront NPF can be added to the FA receiver to improve DR and linearity without sacrificing the sharp filtering offered by FA. Detailed circuit implementation is presented in Section IV, followed by measurement results in Section V. Finally, the conclusions are drawn in Section VI.

II. NC for FA Receiver Front Ends

In this section, we review the LTI NC technique and detail why it is not suited for FA-based receivers, followed by analysis of the proposed PTV-NC.

A. LTI-NC in FA-Based Receivers

A naïve application of LTI-NC to FA leads to the implementation of Fig. 3(a). In the case where $R(t) = 50\ \Omega$, it is essentially identical to FTNC if one were to ignore the sampling of the final output [5], [11]. The noise voltage of $R(t)$, $V_{nR}(t)$, leads to two noise currents through the main and auxiliary NC paths, $i_R(t)$ and $i_{Gm}(t)$, respectively, which are then converted back to voltage at baseband, as shown in Fig. 3(b), where Z_{bb} is the baseband current-to-voltage conversion gain ($= 1/j\omega C$ in the case of FA). It is straightforward to see that, after voltage subtraction, the noise voltage caused by $R(t)$ is nulled at the output, if G_m is selected to be k/R_s with $k = k_2$. If R_s and $R(t)$ are the only noise sources, this renders a perfect 0-dB NF even though $R(t)$ is a time-varying resistor.

However, unfortunately, the sharp filtering is eliminated: by examining Fig. 3(c), which shows how the input signal, $V_s(t)$, is processed, we find that the signal current to be integrated, $i_s(t)$, no longer depends on $R(t)$! This is fundamentally no different from sampling an active-RC integrator.

B. Proposed PTV NC

Instead of the usage of an LTI G_m cell, in [12], we proposed to exploit a PTV $G_m(t)$ cell to sense $V_{nR}(t)$ at node

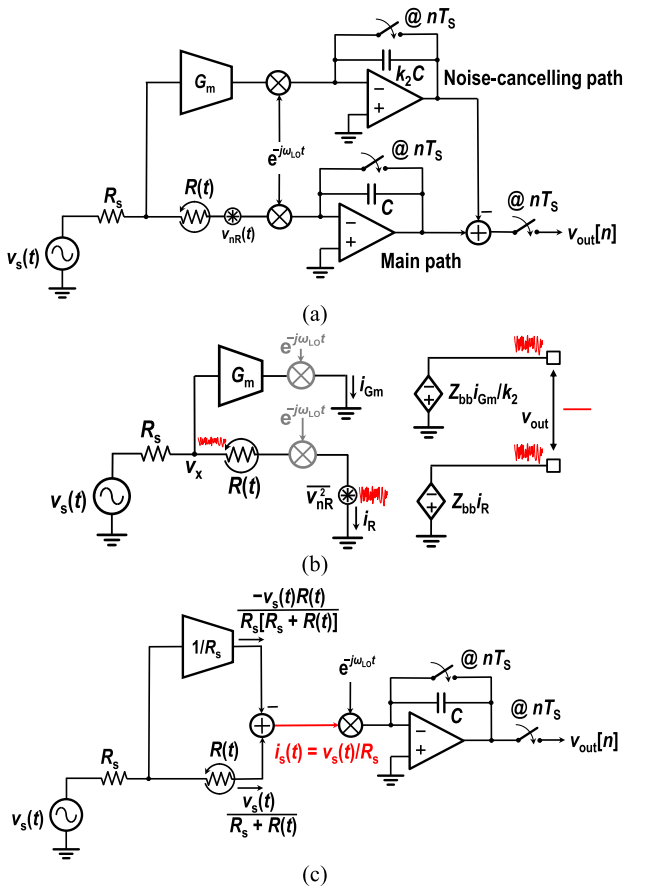

Fig. 3. (a) Block diagram of naïve application of LTI-NC to an FA-based receiver. (b) Simplified model illustrating perfect NC just as in [5] and [11]. (c) Equivalent model for illustration of the destruction of sharp filtering.

V_x, from which the output current is then downconverted, integrated, and sampled to realize the noise-canceling FA path [see Fig. 1(c)]. By replacing the time-invariant G_m cell in Fig. 3(a) with a time-varying one, the signal and the noise now see different filters. The equivalent signal and noise (due to $R(t)$ only) flows in the front end are shown in Fig. 4(a): i_{Gm} and i_R are currents from the G_m cell and through $R(t)$ flowing into their respective virtual grounds, which are later integrated. Fig. 4(b) shows a simplified model that inspects the signal flow of the noise from $R(t)$ only. In contrast to setting $G_m(t) = k/R_s$, we select

$$G_m(t) = \frac{k_1}{R(t)}.$$

Now $i_{nR}(t)$, which is the effective noise current caused by $R(t)$ after cancellation, is not nulled (i.e., the noise from $R(t)$ is not completely canceled as $i_{nR}(t) = 0$ no longer holds). Instead, it becomes $-V_{nR}(t)\{1 - k_1R_s/[k_2R(t)]\}/[R_s + R(t)]$. However, since the noise currents from the two paths, which have the same polarity, are subtracted, the overall noise after integration is still greatly reduced. On the other hand, as shown in Fig. 4(c), the equivalent signal path is almost identical to the FA case. In fact, it is nothing but a scaled version of the original FA filter [due to our choice of $G_m(t)$] with a baseband

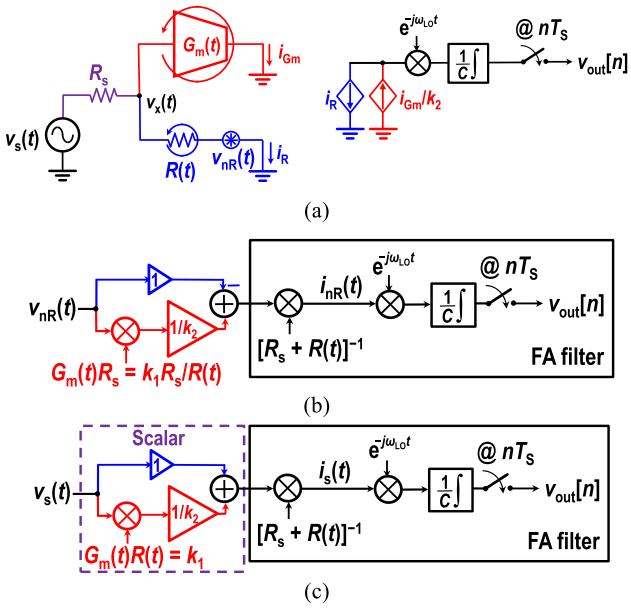

Fig. 4. (a) Equivalent model of the proposed PTV-NC in an FA receiver. (b) Simplified model for noise. (c) Simplified model for signal.

impulse response of

$$g(\tau) = \frac{1 + k_1/k_2}{C[R_s + R(-\tau)]} \tag{3}$$

where $0 \le \tau \le T_s$. Thus, the FA operation is intact, and sharp filtering is achieved. Note (3) is also the effective filter that the source noise sees.

C. Achievable NC

Since perfect NC is not feasible with this approach, it is instructive to consider the theoretically maximum achievable cancellation. Consider the noise factor contribution from $R(t)$: it can be calculated by looking at the autocorrelation of the output voltage samples [9], [10]. Here, we consider the base-band filter only for brevity. It follows from the Appendix that the overall noise factor due to the source and $R(t)$ after cancellation is:

$$F_{PTV} = 1 + F_R = \frac{1 + \lambda^2\left[\overline{G} - \overline{G_{total}}\right]/\overline{G_{total}}}{(1+\lambda)^2} F_{PTV}|_{\lambda=0} \tag{4}$$

where F_R is the noise factor due to $R(t)$, $\lambda = k_1/k_2$ is effectively the gain ratio between the two paths, $\overline{G} = \text{mean}[1/R(t)]$, $\overline{G_{total}} = \text{mean}[1/(R_s + R(t))]$, and $F_{PTV}|_{\lambda=0} = \overline{G_{total}}/(R_s\overline{G_{total}^2})$ is the noise factor without any NC, i.e., the noise factor given in [9, Sec. III-B]. It is unclear, simply by inspecting the expression, what the optimum gain ratio λ ought to be, which can be obtained by setting $\partial F_{PTV}/\partial\lambda = 0$. After simplification, we find

$$\lambda = \frac{k_1}{k_2} = \frac{\overline{G_{total}}}{\overline{G} - \overline{G_{total}}}. \tag{5}$$

Substituting (5) into (4), the minimum achievable noise factor can be found, given by

$$F_{PTV(MIN)} = \frac{\overline{G} - \overline{G_{total}}}{\overline{G}} F_{PTV}|_{\lambda=0}. \tag{6}$$

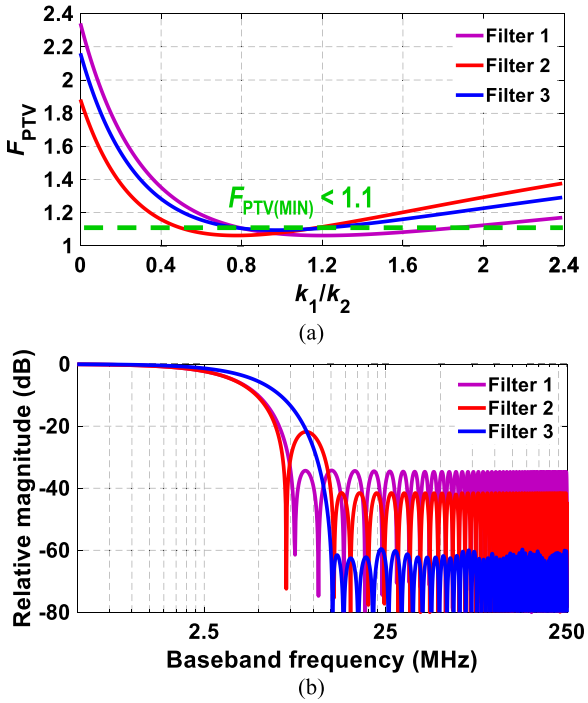

Fig. 5. (a) Noise factor with the PTV-NC for different gain ratio, $\lambda = k_1/k_2$, in three different filter configurations. (b) Corresponding baseband filter frequency responses with $T_s = 200$ ns. Filter 1: transition BW = 1.5× RF BW, $S_{11} \approx$ –10 dB; filter 2: transition BW = 2.5× RF BW, $S_{11} \approx$ –20 dB; filter 3: transition BW = 2.5× RF BW, $S_{11} \approx$ –10 dB (i.e., same as Fig. 2).

It is straightforward to see that, for LTI-NC, $R(t) = R_s$, $F|_{\lambda=0} = 2$, and (5) suggests $\lambda = 1$, plugging which into (4) yields $F = 1$, i.e., perfect NC is achieved. For FA, on the other hand, as expected, the optimum gain ratio, achievable amount of NC, and minimum noise factor depend on $R(t)$. However, (6) does provide us with a bound on $F_{PTV(MIN)}$ due to the minimum value of $R(t)$ in practical implementations. In [9] and [10], it is about 30 Ω. Re-write (6), we obtain

$$F_{PTV(MIN)} = \frac{\int_{t=0}^{T_s} dt/\{R(t)[1+R(t)/R_s]\}}{\int_{t=0_s}^{T_s} dt/R(t)} F_{PTV}|_{\lambda=0} < F_{PTV}|_{\lambda=0}/\left[1+R(t)_{MIN}/R_s\right] = \frac{5}{8} F_{PTV}|_{\lambda=0} \quad (7)$$

for $R_s = 50$ Ω. Given an assumed noise factor of 2 prior to NC,[2] a noise factor better than 1.25 can be achieved after NC. More specifically, for the $R(t)$ variation in Fig. 2, (5) leads to λ of 0.97, which is very close to that in the LTI case. Fig. 5 shows (4) for different values of λ in three different filter configurations, where the blue curves correspond to the $R(t)$ variation shown in Fig. 2. A couple of things are apparent. First, the optimum gain ratio is close to unity. Second, the optimum is fairly shallow suggesting that achievable NC is tolerant to relative gain mismatches between the main and NC paths. Third, the optimum noise factor is actually about 1.1, indicating that about 90% of the noise of $R(t)$ is canceled.

[2]This is a reasonable estimate for *R(t)* variations that lead to meaningful filter shapes and good impedance matching [9], [10], which can be seen from Fig. 5(a) for $k_1/k_2 = 0$, i.e., without NC.

Note until here the only noise sources are R_s and $R(t)$ for simplicity. In practice, with $R(t)$'s noise mostly canceled, $G_m(t)$'s noise becomes important. To evaluate this, an extra term, derived following the Appendix as well, given by:

$$F_{Gm} = \frac{1}{k_1} \frac{\gamma \overline{G(t)}}{R_s(1+1/\lambda)^2 \overline{G_{total}^2(t)}} \quad (8)$$

where γ is the excess noise factor, needs to be added to (4) for the overall noise factor. Such summation can be done due to the fact that the noise from $G_m(t)$ is not correlated with that of $R(t)$ and only appears in the NC path. Since λ is a constant for a given $R(t)$ (≈ 1 in most practical cases), in order to minimize F_{Gm}, k_1 needs to be made large according to (8). In fact, as $k_1 \to +\infty$, the noise contribution from $G_m(t)$ can be made close to zero. However, this will lead to infinite power consumption and infinite baseband capacitor size. Practical selection of k_1 and k_2 is made by making the contribution of $R(t)$ and $G_m(t)$ to be roughly the same, rendering $k_1 = k_2 =\sim 5$ to 6. Here, we only discussed the noises from circuit elements. Other major sources of NF degradation, namely, aliasing and harmonic folding, will be discussed in Section III-D.

An alternative, and maybe more intuitive but not completely mathematically precise, approach to look at how the proposed PTV-NC still effectively cancels the noise is to look at the equivalent filter that $V_{nR}(t)$ sees. For the baseband FA without NC, i.e., main path only, the baseband filter is the same as (1) but with a negative sign. With NC, the baseband filter that $V_{nR}(t)$ sees becomes

$$h(\tau) = -\frac{\lambda R_s - R(-\tau)}{CR(-\tau)[R_s + R(-\tau)]} = g(\tau) - \frac{\lambda R_s}{R(-\tau)} \times g(\tau) \quad (9)$$

where $0 \le \tau \le T_s$. The frequency response of $h(\tau)$ can be found by taking the Fourier transform, given by

$$H(j\Omega) = G(j\Omega) - \lambda \mathcal{F}\left[\frac{R_s}{R(-\tau)}\right] * G(j\Omega) \quad (10)$$

where * is the convolution operator. Note that $G(j\Omega)$ is designed to be a low-pass filter (e.g., Fig. 2). $\mathcal{F}[R_s/R(-\tau)]$ is also low-pass, which means the convolution between $\mathcal{F}[\lambda R_s/R(-\tau)]$ and $G(j\Omega)$ is still low-pass, *albeit* with a larger BW than both filters. There exists λ such that $H(j\Omega) \approx 0$ in the passband, thus rejecting most of the noise from $R(t)$. Since the source noise is not rejected [seen from (3)], the noise factor contribution from $R(t)$ becomes slim, i.e., its noise is canceled.

III. DR and Linearity Enhancement

It is well known that NC can degrade the linearity because of the G_m stage [5]. Similar effect is expected in PTV-NC as well. However, the effect is worse here because V_x sees higher swings. At the RF node, the voltage is

$$V_x(t) = \frac{V_s(t)R(t)}{R_s + R(t)}. \quad (11)$$

Recall the fact that $R(t)$ can be very large at times, e.g., Fig. 2, such that $R(t) \gg R_s$, and hence $V_x(t) \approx V_s(t)$.

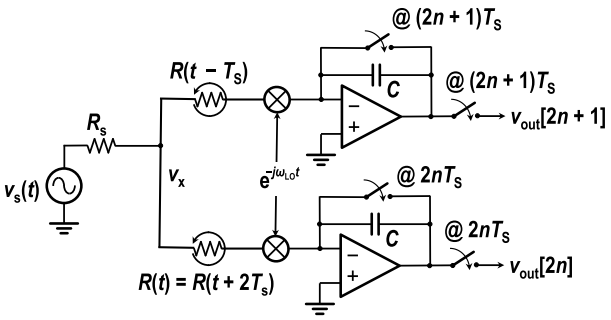

Fig. 6. Time-interleaved FA receiver [10].

If we assume $V_s(t)$ is a simple sinusoid at an arbitrary frequency of interest with an amplitude of A, it is obvious that $V_{x,pk-pk} \approx V_{s,pk-pk} = 2A$. Note this is the case for both in-band and OOB signals since the FA-based receiver has no frequency selectivity at the RF node (as suggested by the ideally frequency-independent S_{11}, which is only somewhat frequency-dependent in practice because of the parasitic capacitance at the RF node) [9], [13]. Consequently, for a big OOB blocker, V_x suffers from large voltage swings that may be outside the voltage range of core MOSFET devices in advanced nodes. In [12], we addressed this by employing TI and an NPF. Here, we analyze their effects and design considerations.

A. Time-Interleaved FA

In [10], time-interleaved FA is used to improve both impedance matching and filter performance. By using two interleaved channels, as shown in Fig. 6, the length of $g(\tau)$ can be doubled, allowing a stopband rejection (A_{stop}) twice as high in theory. In addition, the overall DR of the input resistance seen by the source is less due to the paralleled operation, which is given by $R_{TI}(t) = R(t)||R(t - T_s)$. In the non-TI case, the highest value of $R(t)$ can be a few thousands of Ohms [9]. When TI is used, $\max[R(t)||R(t - T_s)]$ is about 300 Ω. Not only does this makes the input matching easier without having to sacrifice filter shape much for better S_{11} [10], but it slightly reduces $V_{x,pk-pk}$ for the same blocker level. Referring to (11), the swing at V_x is lowered by about 15% (0.5 V for a +10-dBm blocker). Although this only slightly relaxes the DR problem instead of solving it, TI is nonetheless used in this work to achieve better matching and sharper filter at the cost of higher power and larger chip area for two extra paths (one for the main path and one for the NC path).

B. Upfront N-Path Pre-Filtering

An upfront NPF will reduce the swing on V_x and relax the linearity requirements of the NC path [3], [14]. A block diagram of such a combination of an FA receiver, with a time-varying resistor, $\tilde{R}(t)$, and an upfront NPF, is shown in Fig. 7(a).

For in-band signals, the NPF presents a high impedance and has minimal effect on V_x or the current flowing into the PTV resistor, $\tilde{R}(t)$. In contrast, for signals well beyond the NPF's BW, the NPF presents a low impedance, approximately R_{sw},

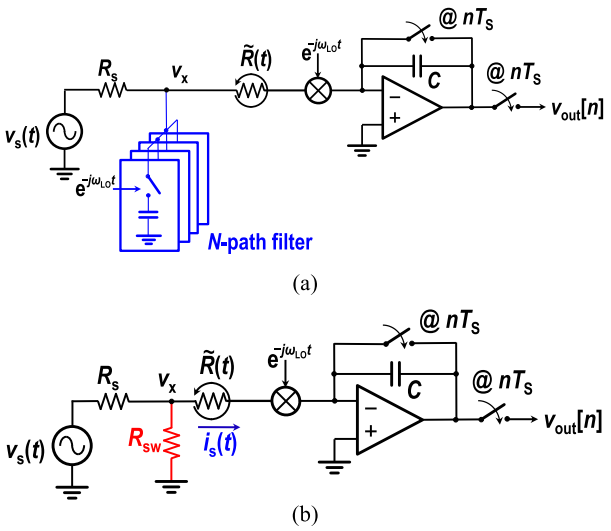

Fig. 7. (a) FA-based receiver with an NPF at the RF node and (b) equivalent circuit for OOB blockers.

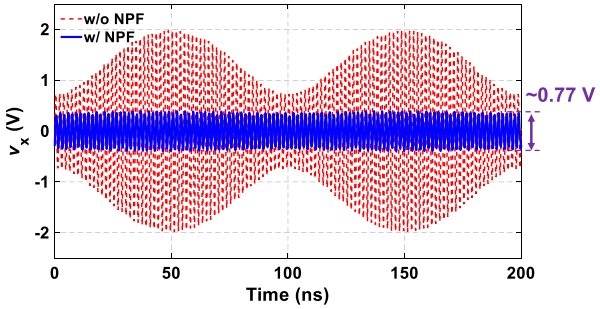

Fig. 8. Simulated voltage waveform at node V_x of the circuit in Fig. 7(a) for a 10-dBm OOB blocker ($\Delta f = 80$ MHz) with and without NPF.

as shown in Fig. 7(b). Since $R_{sw} \ll \tilde{R}(t)$, V_x is effectively much smaller than without the NPF

$$V_x(t) \approx V_s(t)\frac{R_{sw}}{R_{sw} + R_s} = V_s(t)A_{NPF} \tag{12}$$

as desired, where $A_{NPF} = R_{sw}/(R_s + R_{sw})$ is the rejection provided by the NPF. However, the small R_{sw} siphons away much of the signal current from $\tilde{R}(t)$ in a time-varying manner, greatly degrading the effective FA filter shape.

Both effects are readily illustrated using an example $\tilde{R}(t) = R(t)$ designed for 60-dB A_{stop}, 10-MHz RF BW, and 20-MHz transition BW with and without an NPF with 30-MHz BW and 15-dB A_{NPF}. As shown in Fig. 8, the NPF reduces the swing at V_x for a 10-dBm blocker from 4 V to just 0.77 V. However, as is evident from the effective filter responses, without and with the NPF, plotted in Fig. 9, the transition BW is almost doubled even as a higher overall A_{stop} is achieved.

Fortunately, the filter shape degradation can be corrected simply by choosing

$$\tilde{R}(t) = \beta[R_s + R(t)] \tag{13}$$

where $R(t)$ is the PTV resistor variation that ensures the desired filter shape for an FA receiver without the upfront NPF, and β is a constant scaling factor.

Rationale: This choice can be intuitively explained by contrasting Fig. 7(b) with Fig. 1(a), which represents the

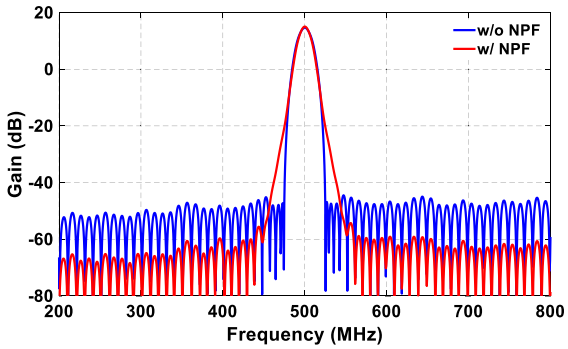

Fig. 9. Simulated frequency responses of the receiver in Fig. 7(a) without and with NPF at $f_{LO} = 500$ MHz [when with the NPF, $\tilde{R}(t) = R(t)$].

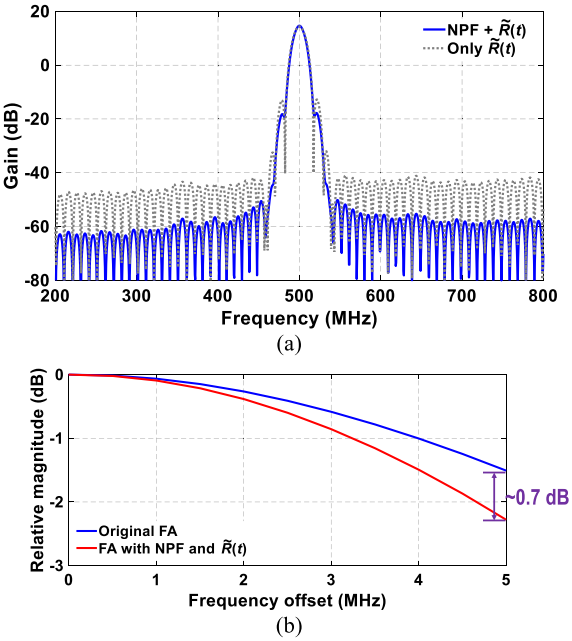

Fig. 10. (a) Simulated frequency response of the receiver with adjusted $\tilde{R}(t)$ values with and without NPF and (b) in-band filter shape comparison between FA without NPF and FA with both NPF and adjusted $\tilde{R}(t)$ values.

desired FA operation without an NPF. It is easy to see that for a signal well beyond the NPF's BW, the current through $\tilde{R}(t)$ in Fig. 7(b) is just a scaled version of the current through $R(t)$ in Fig. 1(a), given by

$$i_s(t) \approx V_s(t) \frac{R_{sw}}{R_{sw} + R_s} \frac{1}{\tilde{R}(t)} = \frac{R_{sw}}{R_{sw} + R_s} \frac{V_s(t)}{\beta[R_s + R(t)]}. \quad (14)$$

Consequently, the OOB filter shape remains effectively the same as what would be achieved without the NPF.

The simulated overall filter shape with (13) is shown in Fig. 10(a). As is evident, most of the filter sharpness is restored (transition BW is only extended by ~6 MHz instead of over 20 MHz, while A_{stop} is a few dB higher than the original FA). The filter shape is primarily defined by FA, while the NPF adds extra rejection at high offset frequencies. Note that this approach results in a slightly larger in-band filter droop, as seen in Fig. 10(b), which is generally acceptable.

Choice of NPF BW and Switch Size: In this work, the NPF BW is chosen to be slightly larger than the desired RF BW of FA. It is, however, worth noting that the actual NPF BW can be chosen to provide more rejection for close-in blockers by using narrower BW in order to meet certain blocker profiles. This comes at having larger overall filter droop, but it can be remedied by re-designing FA to compensate for the extra signal loss by sacrificing some transition BW or A_{stop}. The NPF switch size choice is driven by the tolerable swing at the RF input node, V_x, and the desired OOB IIP_3. Assuming a perfectly linear NPF,[3] with a rejection of A_{NPF}, the intercept point amplitude is approximately $(4|G_m|/3|G_{m3}|)^{1/2}/A_{NPF}$, where G_{m3} is the third-order polynomial coefficient of the transconductance. Therefore, the OOB IIP_3 will be roughly improved by A_{NPF}. In this work, we chose an equivalent 2.5-Ω switch resistance and a BW of 30 MHz for a 10-MHz RF BW configuration to keep the swing at RF within 0.9 V for a +10-dBm blocker and improve the OOB IIP_3 by about 15 dB at 80-MHz offset.

Note also that the NPF changes the effective S_{11} of the FA receiver slightly. A frequency-domain analysis with conversion matrices has been employed before to compute the S_{11} and the effective in-band impedance of an FA receiver [13], [17], [18]. The same approach was extended to the FA + NPF combination described here, after which the scaling factor, β, was chosen to fine-tune the impedance matching.

C. Upfront NPF + TI-FA

Extending the design analysis to TI-FA can be achieved in a similar manner. By recognizing the low impedance presented by the NPF, the OOB signal current flowing through each time-varying resistor can be calculated even when two TI resistors are involved [similar to (14)], and the resistor variations can, therefore, be modified to keep the impulse response a scaled version of the original filter for OOB signals as well. Here, we omit the details for the sake of brevity.

D. Simplified NF Analysis for the Overall Front-End

The noise sources in the NPF (from its switch resistance) are much smaller than other noise sources and can be negligible. Since the overall filter shape is primarily determined by FA [recall Fig. 10(a)], the NPF's effect on the noise spectrum can be ignored. Behavioral simulation results suggest that a discrepancy of less than 0.1 dB in the averaged in-band NF is seen by ignoring these effects.

If TI were not employed, the noise analysis presented in Section II-C could be directly used here simply by replacing $R(t)$ in (4)–(7) with $\tilde{R}(t)$. The effect of TI can be easily approximated by ignoring interactions between the two paths, which is still reasonably viable because the TI channel interaction happens only when $\tilde{R}(t) \approx \tilde{R}(t - T_s)$, which is a short period of time [10], and the correlation between two output samples is small. In this case, the two TI channels contribute independent noise of identical statistics in a TI manner. When combined together, it is as if a single non-TI FA receiver employing a time-varying resistor $\tilde{R}(t)$ [10]. Accordingly, the baseband NF can be determined as $NF_{baseband} = 10\log_{10}(F_{PTV} + F_{Gm})$.

[3]This is a fair assumption since the NC path dominates the non-linearity.

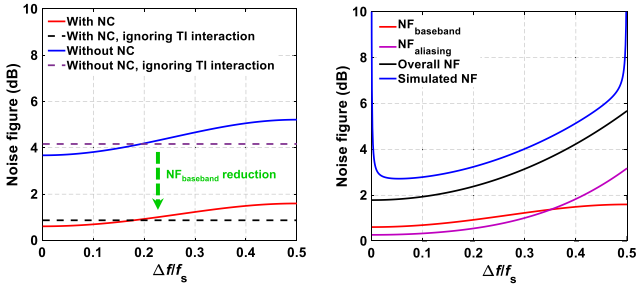

Fig. 11. (a) Comparison of the calculated $\mathrm{NF_{baseband}}$ with and without NC and (b) calculated $\mathrm{NF_{baseband}}$, $\mathrm{NF_{aliasing}}$, and calculated and simulated overall NF with $f_{\mathrm{LO}} = 500$ MHz with both NC and NPF ($\beta = 0.54$).

However, the TI channels do interact, resulting in correlation between samples of the output noise. This effect has been described in [10] for a system without NC. Similar calculations can be performed here (see the Appendix) to calculate the precise NF contribution of the input matching resistors and G_{m} cells. The resultant $\mathrm{NF_{baseband}}$ is now a function of the baseband frequency, Δf, where $|\Delta f| \leq 1/(2T_{\mathrm{s}})$. Fig. 11(a) plots the calculated NF with and without NC for both the cases where the TI channel interaction is considered (solid curves) and ignored (dashed curves). The approximation ignoring the TI interaction only introduces a small error on $\mathrm{NF_{baseband}}$, *albeit* making it frequency-independent. The average in-band $\mathrm{NF_{baseband}}$ error is less than 0.2 dB with approximation. In either case, NC is observed and the average $\mathrm{NF_{baseband}}$ is lowered by about 3 dB. In our calculation, the baseband amplifiers' noises are taken care of in two means: 1) the amplifiers in the main path present themselves as part of $\tilde{R}(t)$ and $\tilde{R}(t - T_{\mathrm{s}})$ [10], and their noises get mostly canceled and 2) those in the NC path still present their noises but they are suppressed due to the gain of the G_{m} cells just as in [5] (moreover, the baseband amplifiers in this work are designed to have large g_{m}). The passive mixers' switch noises are considered similarly: 1) main-path mixer's switch noise gets mostly canceled and 2) the NC-path mixer contributes little noise.

In addition to $\mathrm{NF_{baseband}}$, two additional sources also contribute to the overall NF, namely the aliasing of the source noise as a result of sampling at the output and harmonic folding due to the N-path operation. They are given by [9]

$$\begin{aligned} \mathrm{NF_{aliasing}}(\Delta f) &= \frac{\mathrm{PSD_{Rs}}(\Delta f)}{2kTR_{\mathrm{s}}|G(\Delta f)|^2} \\ &= \frac{\sum_{n=-\infty}^{+\infty}|G(\Delta f + nf_{\mathrm{s}})|^2}{|G(\Delta f)|^2} \\ \mathrm{NF_{harmonics}} &= \frac{1}{\mathrm{sinc}^2(1/N)} \approx 0.91 \text{ dB} \end{aligned} \tag{15}$$

where $\mathrm{PSD_{Rs}}(\Delta f)$ is the power spectral density due to noise from R_{s}, $f_{\mathrm{s}} = 1/T_{\mathrm{s}}$ is the sampling rate at the output, $G(f)$ is the frequency response of the filter, $g(\tau)$, and N is the number of paths in the NPF and mixer, which is 4 in our implementation. Note $\mathrm{PSD_{Rs}}(\Delta f)$ can also be computed by looking at the autocorrelation of the output sampled voltages [10].

Finally, the overall NF at a certain Δf for the complete system can be derived as

$$\mathrm{NF_{total}}(\Delta f) = \mathrm{NF_{baseband}}(\Delta f) + \mathrm{NF_{aliasing}}(\Delta f) + \mathrm{NF_{harmonics}}. \tag{16}$$

The calculated NF with PTV-NC and NPF is shown in Fig. 11(b) in comparison with the simulated results.[4] With both NC and NPF, the calculated $\mathrm{NF_{min,IB}}$ is 1.8 dB and $\mathrm{NF_{avg,IB}}$ is 3.2 dB. The simulation results agree well with calculation, except for an extra NF degradation of about 0.8 dB mostly due to the loss caused by input parasitic capacitance [13]. The peaking close to dc is due to flicker noise, and as a consequence of the TI operation, half of the flicker noise power being shifted up to $f_{\mathrm{s}}/2$ is observed, similar to [10].

IV. Circuit Implementation

Fig. 12 shows the block diagram of the implemented PTV-NC receiver front end. The values of k_1 and k_2 are programmable but are roughly set to 5–6 by design for best tradeoff between $G_{\mathrm{m}}(t)$'s noise contribution and area. The receiver front end consists of only switches, inverter-based amplifiers, digital circuits, and passive devices (namely, resistors and capacitors).

$R_{1,2}(t)$ are implemented as two 13-bit binary resistor DACs (RDACs) [see Fig. 13(a)]. The switches are implemented by transmission gates with equally sized pFETs and nFETs, and the resistors are made of high-resistive polysilicon. Both are binary scaled in the RDACs. In this work, the linearity is primarily limited by the NC path. Therefore, in contrast to prior implementation of FA-based receivers where it is sized such that the resistance ratio between the transmission gate and the polysilicon resistor is 1:4, this work uses a ratio of 1:1, and minimum-sized (both width and length) transmission gates are used, lowering the parasitic capacitance due to the RDACs. The RDACs are designed to have a minimum resistance of 30 Ω. $G_{\mathrm{m1,2}}(t)$ are formed by inverter-based G_{m} cells binarily turned ON/OFF by switches (G_{m}DACs), shown in Fig. 13(b), which is similar to that in [19], *albeit* being a higher power one. Switches in the G_{m}DACs act as source-degeneration resistors to the G_{m} cells and are, therefore, designed to contribute less than 10% of the effective g_{m} in each cell for noise consideration. Non-minimum-length devices are used in the G_{m} cells (one unit cell has an equivalent W/L of 140 nm/55 nm) for lower γ and higher output resistance at the cost of more degradation on both S_{11} and NF at high frequencies. The finite output resistances of the G_{m} cells degrade the NF slightly and would be more if minimum-length devices are used. The linearity is primarily limited by the G_{m} cells, and no special techniques were employed to reduce the non-linearity of the G_{m} cells except to keep both the baseband input impedance and the mixer switch resistance small in order to reduce the effects from g_{ds} non-linearity, similar to [5]. The RDACs and G_{m}DACs all vary at the rate of a clock frequency, f_{clk}, which is also used to generate all sampling and reset control clocks.

[4]The simplified analysis model without actually introducing the NPF is used for calculation only, not for simulations.

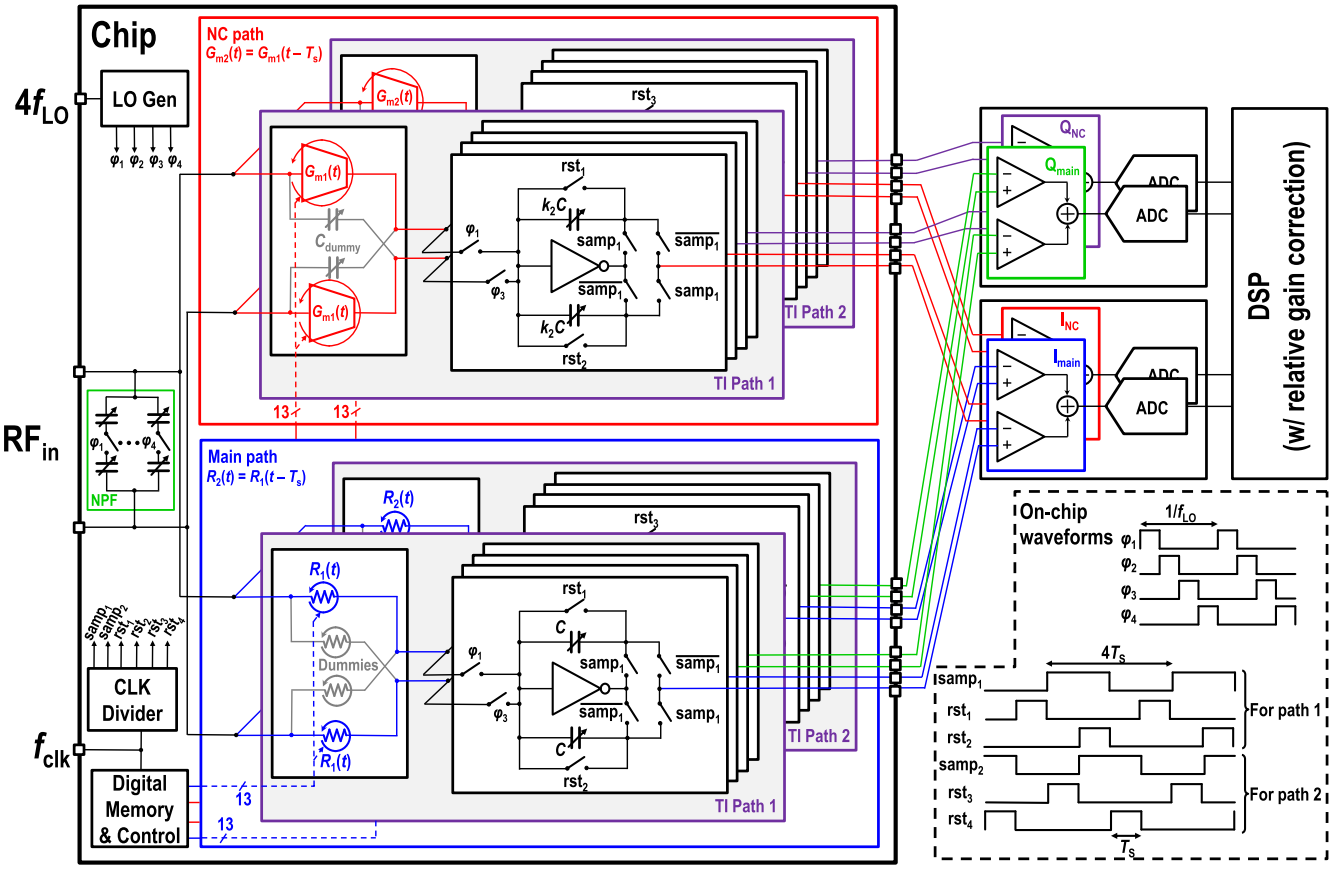

Fig. 12. Complete block diagram of the implemented receiver front end.

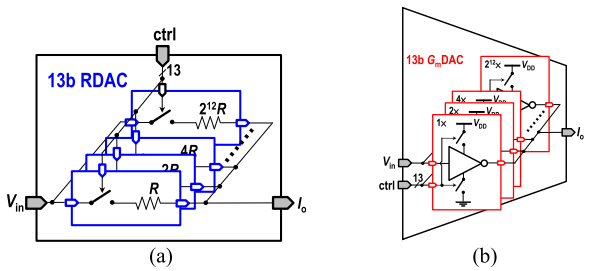

Fig. 13. Realization of (a) RDAC and (b) G_mDAC.

The bias of the entire chain is set to about half of the supply voltage, V_{DD}, by resetting baseband amplifiers, which also define the voltages at the input and the output of the G_mDACs via the main and NC paths, respectively. No dedicated biasing circuitry is used. These baseband amplifiers are sized to have 125-mS g_m and 35-dB dc gain each with ping-pong capacitor banks around them for sampling. Similar to [9] and [10], the baseband amplifier's g_m is in fact part of $R(t)$ and is thus made large. The baseband integrator capacitors are tunable from 10 to 70 pF in the main path and 50 to 350 pF in the NC path.

Switches in the 4-path mixer and NPF are sized for ON-resistances of 2.5 and 5 Ω, respectively. Here, for having better linearity on the NPF and reduce the effective switch resistance, the bottom-plate mixing version of NPF [14] is used in both simulations and implementation of this work at the cost of higher input parasitic capacitance. The effective switch resistance of the NPF is, therefore, 2.5 Ω by design. Since both the G_m cells and the NPF add additional capacitance to the input node that limits S_{11} at high carrier frequencies, whereas the former is also observed in the LTI-NC case, the top-plate mixing NPF may be used instead to improve high-frequency performance but worsens the OOB IIP_3 by a couple dBm according to simulations. Nevertheless, it still resolves the OOB DR and linearity issue. Note that in this work, the mixer switches in the main path are large to accommodate the variation of $R(t)$, while in LTI-NC, since the noise from these switches is canceled, they can be much smaller to save LO power. The NPF and the mixers are driven by the same set of 25% duty-cycle clocks at f_{LO}.

V. Measurement Results

The implemented test chip was fabricated in a 28-nm CMOS process. Fig. 14 shows the die photo of the chip. The active area is 3.75 mm^2, 90% of which is occupied by baseband capacitors. Note the capacitor area can be significantly reduced when designed for operations with only higher RF BWs. The supply voltage of the whole chip is 0.9 V. At $f_{LO} = 500$ MHz, the entire chip consumes 61-mW power. Each baseband amplifier consumes about 2.7 mA, the LO divider and switch drivers consume about 16 mA, in which the NPF drivers consume about 1 mA, and the digital control circuitry dissipates 5.2 mA at a nominal f_{clk} of 1 GHz. It has been verified to work with an f_{clk} up to 2 GHz. On average, each G_mDAC consumes roughly 2-mA current. The power

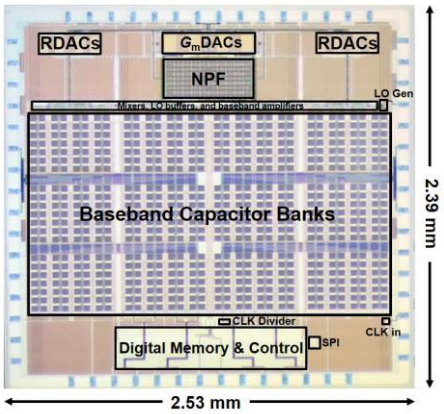

Fig. 14. Chip micrograph.

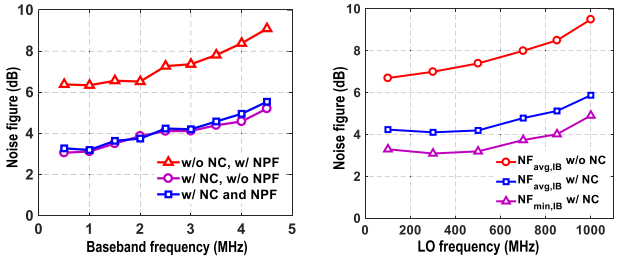

Fig. 15. (a) Measured in-band NFs with and without NC with $f_{LO} = 500$ MHz and RF BW $= 10$ MHz (5-MHz baseband BW). (b) NF across different LO frequencies.

increases with f_{LO} due to LO divider and switch drivers being more power hungry at higher frequencies. The sampled outputs are buffered externally, converted into digital signals by off-chip ADCs, and then processed digitally for signal summation and subtraction, with relative gain correction similar to that in [20]. The filter responses are generated by providing tonal inputs and then measuring the downconverted and aliased signals at baseband after sampling, similar to other FA works [8]−[10] (see [8, Sec. V] for more details). The RDACs and G_mDACs are dc calibrated at startup [9].

Fig. 15(a) and (b) shows the measured in-band NF at 500-MHz f_{LO} and the measured NF with and without NC at different LO frequencies, respectively. With both NPF and NC, the $NF_{min,IB}$ is 3.2 dB and the averaged NF over [0, $f_s/2$), $NF_{avg,IB}$, is 4.2 dB. The increase of in-band NF at higher offset frequencies is due to filter droop, as seen in Fig. 11. It is also observed that the NPF does have minimal impact on the NF. Without the NPF, $NF_{avg,IB}$ is about 0.15 dB better. In contrast, both $NF_{min,IB}$ and $NF_{avg,IB}$ are about 3-dB worse without NC.

The measured A_{stop} for the overall filter is greater than 67 dB for a transition BW of 40 MHz with a gain of ∼30 dB, as shown in Fig. 16(a), for 10-MHz RF BW. The achieved A_{stop} and transition BW are similar to [10] with 46- and 58-dB rejection at 22- and 30-MHz offset (using the same 67-dB A_{stop} configuration). This indicates that filter performance is preserved well with PTV-NC and NPF. The filter can be programed to have 2.5–40-MHz RF BW, shown in Fig. 16(b). Fig. 16(c) shows the filter responses with f_{LO} varied from 100 MHz to 1 GHz.

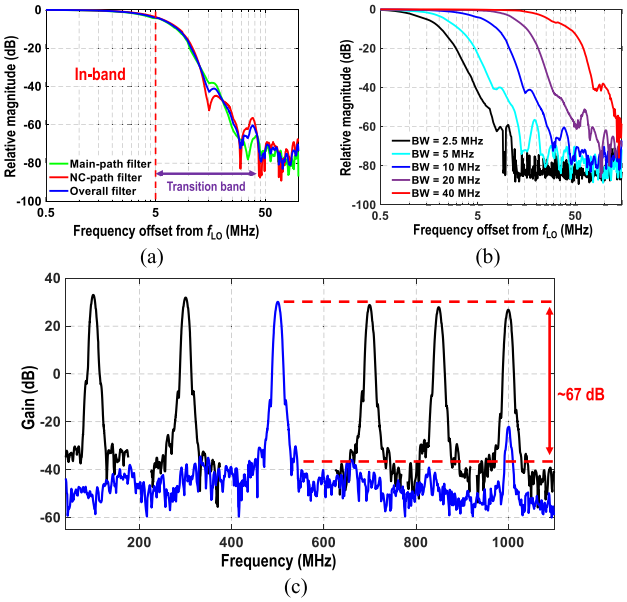

Fig. 16. (a) Measured 10-MHz RF BW filter responses. (b) Filter responses with BW tuned from 2.5–40 MHz. (c) Filter responses for LO frequency varied from 0.1–1 GHz.

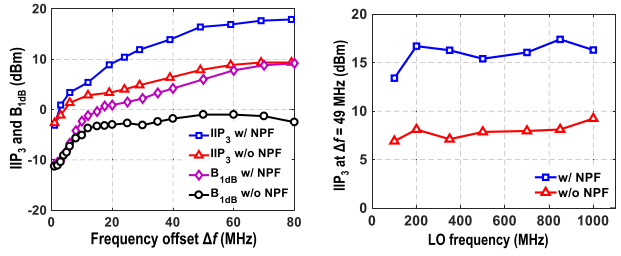

Fig. 17. (a) Measured IIP_3 and B_{1dB} with and without NPF for $f_{LO} = 500$ MHz. (b) OOB IIP_3 at 49-MHz offset for different LO frequencies.

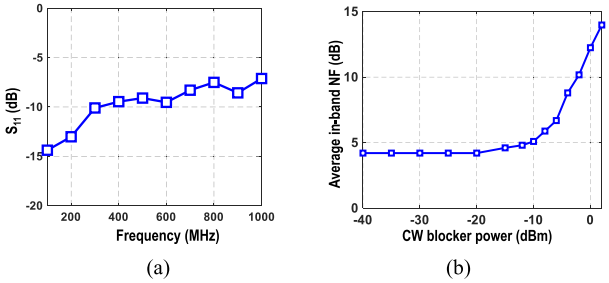

Fig. 18. (a) Measured S_{11} and (b) blocker NF in the presence of a CW blocker at $\Delta f = 30$ MHz with $f_{LO} = 500$ MHz.

The linearity performance, i.e., B_{1dB} and IIP_3, against different frequency offset and f_{LO} of the receiver in the 10-MHz RF BW configuration are depicted in Fig. 17. An OOB IIP_3 of +18 dBm and an OOB B_{1dB} of +9 dBm are achieved even with upfront G_mDACs and 0.9-V supply, thanks to the NPF. Without the NPF, both OOB B_{1dB} and IIP_3 evidently degrade by about 9 dB. The measured S_{11} and blocker NF are given in Fig. 18. $NF_{avg,IB}$ is 12 dB with a 0-dBm continuous-wave (CW) blocker placed at 30-MHz offset. It is primarily limited by the phase noise of the LO divider, which has a simulated phase noise of −164 dBc/Hz at 30-MHz offset. Better blocker

TABLE I
PERFORMANCE SUMMARY AND COMPARISON WITH THE STATE OF THE ART

	[5] JSSC'12	[6] JSSC'16	[10] JSSC'18	[14] JSSC'19	[15] JSSC'19	[22] JSSC'18	[23] JSSC'20	**This work**
Architecture	FTNC	*N*-path + DT filtering	TI-FA	*N*-path	*N*-path	*N*-path	*N*-path	**TI-FA + PTV-NC + *N*-path**
Technology	40 nm	65 nm	65 nm	28 nm	65 nm	45 nm SOI	28 nm	**28 nm**
RF frequency (GHz)	0.08–2.7	0.1–0.7	0.1–1	0.1–2	0.8–1.1	0.2–8	0.2–2	**0.1–1**
RF input	Single-ended	Differential	Differential	Differential	Differential	Differential	Single-ended	**Differential**
Bandwidth† (MHz)	4	6.4–9.6	2.5–40	13	30–50	20	18	**2.5–40**
A_{stop} (transition BW)	N/A	>70 dB (8.5× BW)	>45 dB (1.7× BW) >70 dB (4× BW)	>47* dB (6× BW)	>15* dB (0.5× BW)	>25 dB (4.5× BW)	~28* dB (2.8× BW)	**>46 dB (1.7× BW) >67 dB (4× BW)**
$NF_{min,IB}$ (dB)	1.9	6.8–9.7#	6# @ 0.5 GHz	4.1–10.3#	5.0–8.6#	2.3–7.2*#	4.3–7.6	**3.1–4.9#**
$NF_{avg,IB}$ (dB)	N/A	N/A	6.5–8.5#	N/A	~7.6–9*#	N/A	N/A	**4.1–5.8#**
OOB IIP_3 (dBm)	+13.5 (20× BW)	+24 (4.7× BW)	+24 (4× BW)	+44 (12.3× BW)	+24 (1× BW)	+39 (4× BW)	+33 (4.4× BW)	**+18 (8× BW)**
OOB B_{1dB} (dBm)	−2 (20× BW)	+14.7 (4.7× BW)	+13 (4× BW)	+13 (12.3× BW)	+9 (1× BW)	+12 (4× BW)	+12 (3.3× BW)	**+9 (8× BW)**
OOB IIP_2 (dBm)	+55	N/A	+64	+90	+61	+88	N/A	**+65**
Gain (dB)	72	40	23	16	−5*	21	13	**30**
Supply voltage (V)	1.3	1.2/1.6	1.2/1	1.2/1.0	1	1.2/1	1.2	**0.9**
Power (mW)	35–78	59–105	75–99	38–96	80–97	56–290	146.6–179	**48–74**
Area (mm^2)	1.2	1.2	2.3	0.49	1.9	0.8	0.48	**3.75**

*Estimated from figures #Excludes balun loss †RF bandwidth

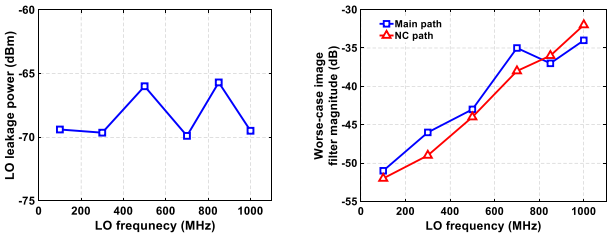

(a) (b)

Fig. 19. (a) Measured LO leakage power and (b) worst case image filter magnitude at different LO frequencies.

NF should be achievable by burning more power in the LO divider.

Fig. 19 shows the measured LO leakage power and worst case image filter (normalized to the peak of the corresponding desired filter frequency responses) at different LO frequencies. Due to the N-path operation of the NPF and the mixers plus the lack of an isolating LNA after the antenna, the LO leakage power is about −65 to −70 dBm, which is similar to other N-path-based or mixer-first architectures [21]. The image filter is caused by the TI path mismatches and degrades at higher LO frequencies due to LO clock skews [10]. The worst case image rejection is better than 30 dB, sufficient for most SNR requirements. Other than filter shapes, other metrics do not vary appreciably for different configurations.

Table I compares this work with the state of the art. While it maintains very sharp filtering with narrow transition band and high A_{stop} of FA [10], the NF compares more favorably against other works compared with [10]. Good OOB linearity is demonstrated with a 0.9-V supply, while all other works use higher supply voltages, mostly in the range of 1.2–1.6 V. Since this work relies on NPF to improve the linearity rather than linear resistors, close-in linearity is worse than [10]. It may be noted that unlike traditional architectures [5], [14], [15], [22], [23], where further filtering can be done on adjacent channels, the FA system as presented here allows folding of transition band signals into passband without full suppression, which is detrimental in a congested spectrum. To prevent such folding, the FA filter can be designed to have a lower BW while maintaining the sampling rate to ensure that the passband is free of folding artifacts, but this places an upper limit on the allowable transition BW (and hence A_{stop}). To increase the allowable transition BW and, therefore, higher rejection while maintaining signal BW, the effective output sampling rate needs to be increased. This generally requires more TI.

VI. CONCLUSION

In this article, we detailed a PTV NC technique for FA-based receiver. It realizes both sharp filtering and low NF by employing PTV resistors and G_m cells. Both minimum and averaged in-band NFs are improved by about 3 dB by the proposed technique. The stopband rejection is better than 67 dB for a transition BW of four times the RF BW. OOB linearity is preserved well by introducing an NPF that helps the NC path better handle the OOB blockers, while in-band linearity is worsened due to the presence of active devices at RF.

APPENDIX
GENERALIZED NOISE ANALYSIS FOR BASEBAND FA

We present a generalized analysis to calculate the noise factor contribution from each circuit component here. The fundamental principles are the same as in [9], but more general.

For a particular noise voltage, $V_n(t)$, consider it goes through an equivalent baseband filter by multiplying $V_n(t)$ with a PTV conductance, $D_n(t)$, and then integrating the current with a capacitor C. The equivalent model is depicted

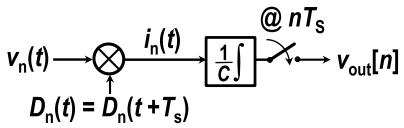

Fig. 20. Model for a general noise source $V_n(t)$.

in Fig. 20. The sampled output becomes

$$V_{out}[n] = \int_{t=(n-1)T_s}^{nT_s} \frac{V_n(t)D_n(t)}{C}dt \tag{17}$$

from which the autocorrelation of the output voltage samples, $R_{oo}[m,n]$, can be calculated. As $D_n(t)$ is periodic with a period of T_s, $R_{oo}[m,n]$ is wide-sense stationary and is given by [9]

$$\begin{aligned} R_{oo}[m,n] &= R_{oo}[m-n] = R_{oo}[l] = E[V_{out}[m]V_{out}[n]] \\ &= E\left[\frac{1}{C^2}\int_{t_1=(m-1)T_s}^{mT_s}\int_{t_2=(n-1)T_s}^{nT_s} V_n(t_1)V_n(t_2) \right. \\ &\qquad \left. \times D_m(t_1)D_n(t_2)dt_1dt_2\right] \end{aligned} \tag{18}$$

where $D_m(t)$ and $D_n(t)$ are the time-varying conductances for $V_{out}[m]$ and $V_{out}[n]$, respectively. For non-TI-FA, they are identical, but for TI-FA, as will be shown later, they are not necessarily the same. If we assume the noise source to be white Gaussian with autocorrelation

$$R_{nn}(t_1,t_2) = E[V_n(t_1)V_n(t_2)] = 2kTR_n(t_1)\delta(t_1-t_2) \tag{19}$$

where k is the Boltzmann constant, T is the temperature in Kelvin, and $\delta(.)$ is the Dirac delta function, then we find that (18) can be expressed as

$$R_{oo}[l] = \frac{2kT}{C^2}\int_{t_1=(m-1)T_s}^{mT_s}\int_{t_2=(n-1)T_s}^{nT_s} R_n(t)D_m(t_1)D_n(t_2)dt_1dt_2 \tag{20}$$

which for the non-TI case can be simplified into

$$R_{oo}[0] = \frac{2kT}{C^2}\int_{t=0}^{T_s} R_n(t)[D(t)]^2dt \tag{21}$$

and $R_{oo}[l] = 0$ when $l \neq 0$. The only remaining unknown factor $D(t)$ can be found with the equivalent models like Fig. 4(c) using simple KCL/KVL analyses. From (21), the overall output noise voltage autocorrelation can be easily computed with superposition since the noise sources, i.e., R_s, $R(t)$, and $G_m(t)$, are independent. For the circuit in Fig. 4(a), we consider the noise sources to be white Gaussian with autocorrelations

$$\begin{aligned} R_{ss}(t_1,t_2) &= E[V_s(t_1)V_s(t_2)] = 2kTR_s\delta(t_1-t_2) \\ R_{nRnR}(t_1,t_2) &= E[V_{nR}(t_1)V_{nR}(t_2)] = 2kTR(t_1)\delta(t_1-t_2). \end{aligned} \tag{22}$$

By inspecting Fig. 4(b) and (c), we find that for the noise from R_s, $D(t) = (1+k_1/k_2)/[R_s+R(t)]$, and for the noise from $R(t)$, $D(t) = -\{1-k_1R_s/[k_2R(t)]\}/[R_s+R(t)]$. Then, the overall autocorrelation can be given by

$$\begin{aligned} R_{oo}[0] = &\frac{2kT}{C^2}\int_{t=0}^{T_s}\frac{R_s(1+k_1/k_2)^2}{[R_s+R(t)]^2}dt \\ &+\frac{2kT}{C^2}\int_{t=0}^{T_s}\frac{R(t)\{1-k_1R_s/[k_2R(t)]\}^2}{[R_s+R(t)]^2}dt \end{aligned} \tag{23}$$

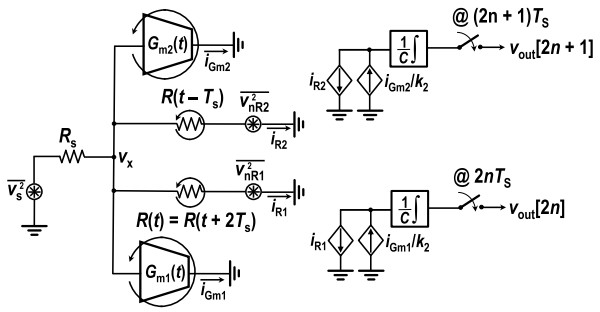

Fig. 21. Simplified model for calculating $D_n(t)$ for PTV-NC with TI (ignoring $G_{m1,2}(t)$'s noise).

and $R_{oo}[l] = 0$ when $l \neq 0$. The corresponding PSD can be found

$$S_{oo}(e^{j\omega}) = R_{oo}[0]. \tag{24}$$

By dividing (23) by its first term, which is the source noise seen at the output of the filter, we obtain (4) after simplification.

Considering the noise from the $G_m(t)$ cell is simple too, which is considered to have an input-referred noise with autocorrelation [as $G_m(t) = k_1/R(t)$]

$$R_{GmGm}(t_1,t_2) = E[V_{Gm}(t_1)V_{Gm}(t_2)] = \frac{2kT\gamma R(t_1)\delta(t_1-t_2)}{k_1} \tag{25}$$

and the corresponding $D(t) = G_m(t)/k_2 = k_1/[k_2R(t)]$. This leads to

$$S_{oo}(e^{j\omega}) = R_{oo}[0] = \frac{2kT}{C^2}\int_{t=0}^{T_s}\frac{\gamma k_1}{k_2^2R(t)}dt. \tag{26}$$

Dividing (26) with the first term in (23) leads to (8), which is the noise factor that $G_m(t)$ contributes.

Extending (20) to TI-FA is the same with an exception of $R_{oo}[l] \neq 0$ for some l. Ignoring NPF, PTV-NC with TI can be simplified into Fig. 21 (mixer is omitted for baseband noise calculation), similar to Fig. 4(a). Here, $G_{m1}(t) = k_1/R(t)$ and $G_{m2}(t) = k_1/R(t-T_s)$. Consider the noise from $R(t)$, $V_{nR1}(t)$, with an autocorrelation of $2kTR(t_1)\delta(t_1-t_2)$, (20) can be rewritten into

$$R_{oo}[l] = \begin{cases} \dfrac{2kT}{C^2}\displaystyle\int_{t=0}^{2T_s} R(t)[D_0(t_1)]^2dt & l=0 \\ \dfrac{2kT}{C^2}\displaystyle\int_{t=0}^{T_s} R(t)D_0(t)D_1(t)dt & l=\pm1 \\ 0 & \text{else} \end{cases} \tag{27}$$

where the corresponding time-varying conductances, $D_0(t)$ and $D_1(t)$, can be again found by building equivalent models for the output samples similar to Fig. 4(c). They are given by

$$\begin{aligned} D_0(t) &= \frac{\lambda R_s||R(t-T_s)/R(t)-1}{R(t)+R_s||R(t-T_s)} \quad \text{for } V_{out}[2n] \\ D_1(t) &= \frac{(1+\lambda)R_s||R(t-T_s)}{R(t-T_s)\times[R(t)+R_s||R(t-T_s)]} \quad \text{for } V_{out}[2n\pm1]. \end{aligned} \tag{28}$$

Subsisting (28) with $\lambda = 0$, i.e., without NC, into (27) gives exactly the last term of (9) in [10]. Noise from other sources can be computed the same way, and the noise factor with NC

can be calculated by taking the Fourier transform of $R_{oo}[l]$ after considering all noise sources to obtain the PSD with proper λ. As for the two G_m cells' noises, the corresponding autocorrelations of output voltages are single tap, since the noise from $G_{m1}(t)$ [or $G_{m2}(t)$] only appears in its own path and is uncorrelated. The resultant NF due to them is flat across the band. It can be calculated the same way as the non-TI case.

ACKNOWLEDGMENT

The authors would like to thank MaxLinear, Inc. for silicon donation and tapeout support.

REFERENCES

[1] A. A. Abidi, "The path to the software-defined radio receiver," *IEEE J. Solid-State Circuits*, vol. 42, no. 5, pp. 954–966, May 2007.
[2] M. Nekovee, "Cognitive radio access to TV white spaces: Spectrum opportunities, commercial applications and remaining technology challenges," in *Proc. IEEE Symp. New Frontiers Dyn. Spectr. (DySPAN)*, Apr. 2010, pp. 1–10.
[3] A. Ghaffari, E. A. M. Klumperink, M. C. M. Soer, and B. Nauta, "Tunable high-Q N-path band-pass filters: Modeling and verification," *IEEE J. Solid-State Circuits*, vol. 46, no. 5, pp. 998–1010, May 2011.
[4] C. Andrews and A. C. Molnar, "A passive mixer-first receiver with digitally controlled and widely tunable RF interface," *IEEE J. Solid-State Circuits*, vol. 45, no. 12, pp. 2696–2708, Dec. 2010.
[5] D. Murphy *et al.*, "A blocker-tolerant, noise-cancelling receiver suitable for wideband wireless applications," *IEEE J. Solid-State Circuits*, vol. 47, no. 12, pp. 2943–2963, Dec. 2012.
[6] Y. Xu and P. R. Kinget, "A switched-capacitor RF front end with embedded programmable high-order filtering," *IEEE J. Solid-State Circuits*, vol. 51, no. 5, pp. 1154–1167, May 2016.
[7] M. Rachid, S. Pamarti, and B. Daneshrad, "Filtering by aliasing," *IEEE Trans. Signal Process.*, vol. 61, no. 9, pp. 2319–2327, May 2013.
[8] N. Sinha, M. Rachid, S. Pavan, and S. Pamarti, "Design and analysis of an 8 mW, 1 GHz span, passive spectrum scanner with $> +31$ dBm out-of-band IIP3 using periodically time-varying circuit components," *IEEE J. Solid-State Circuits*, vol. 52, no. 8, pp. 2009–2025, Aug. 2017.
[9] S. Hameed and S. Pamarti, "Design and analysis of a programmable receiver front end based on baseband analog-FIR filtering using an LPTV resistor," *IEEE J. Solid-State Circuits*, vol. 53, no. 6, pp. 1592–1606, Jun. 2018.
[10] S. Hameed and S. Pamarti, "Design and analysis of a programmable receiver front end with time-interleaved baseband analog-FIR filtering," *IEEE J. Solid-State Circuits*, vol. 53, no. 11, pp. 3197–3207, Nov. 2018.
[11] F. Bruccoleri, E. A. M. Klumperink, and B. Nauta, "Wide-band CMOS low-noise amplifier exploiting thermal noise canceling," *IEEE J. Solid-State Circuits*, vol. 39, no. 2, pp. 275–282, Feb. 2004.
[12] S. Bu, S. Hameed, and S. Pamarti, "An LPTV noise cancellation technique for a 0.9-V filtering-by-aliasing receiver front-end with $>$ 67-dB stopband rejection," in *Proc. IEEE Custom Integr. Circuits Conf. (CICC)*, Austin, TX, USA, Apr. 2019, pp. 1–4.
[13] S. Hameed and S. Pamarti, "Impedance matching and reradiation in LPTV receiver front-ends: An analysis using conversion matrices," *IEEE Trans. Circuits Syst. I, Reg. Papers*, vol. 65, no. 9, pp. 2842–2855, Sep. 2018.
[14] Y.-C. Lien *et al.*, "High-linearity bottom-plate mixing technique with switch sharing for N-path filters/mixers," *IEEE J. Solid-State Circuits*, vol. 54, no. 2, pp. 323–335, Feb. 2019.
[15] P. Song and H. Hashemi, "RF filter synthesis based on passively coupled N-path resonators," *IEEE J. Solid-State Circuits*, vol. 54, no. 9, pp. 2475–2486, Sep. 2019.
[16] G. Qi *et al.*, "A 0.7 to 1 GHz switched-LC N-path LNA resilient to FDD-LTE self-interference at $\geq$40 MHz offset," in *Proc. IEEE Radio Freq. Integr. Circuits Symp. (RFIC)*, Honolulu, HI, USA, Jun. 2017, pp. 276–279.
[17] S. Hameed, M. Rachid, B. Daneshrad, and S. Pamarti, "Frequency-domain analysis of N-path filters using conversion matrices," *IEEE Trans. Circuits Syst. II, Exp. Briefs*, vol. 63, no. 1, pp. 74–78, Jan. 2015.
[18] S. Hameed, M. Rachid, B. Daneshrad, and S. Pamarti, "Frequency-domain analysis of a mixer-first receiver using conversion matrices," in *Proc. IEEE Int. Symp. Circuits Syst. (ISCAS)*, May 2015, pp. 541–544.
[19] B. J. Thijssen, E. A. M. Klumperink, P. Quinlan, and B. Nauta, "A 0.06–3.4-MHz 92-μW analog FIR channel selection filter with very sharp transition band for IoT receivers," *IEEE Solid-State Circuits Lett.*, vol. 2, no. 9, pp. 171–174, Sep. 2019.
[20] Y. Zhang, J. Zhu, and P. R. Kinget, "An out-of-band IM3 cancellation technique using a baseband auxiliary path in wideband LNTA-based receivers," *IEEE Trans. Microw. Theory Techn.*, vol. 66, no. 6, pp. 2580–2591, Jun. 2018.
[21] S. Jayasuriya, D. Yang, and A. Molnar, "A baseband technique for automated LO leakage suppression achieving < -80dBm in wideband passive mixer-first receivers," in *Proc. IEEE Custom Integr. Circuits Conf. (CICC)*, San Jose, CA, USA, Sep. 2014, pp. 1–4.
[22] Y.-C. Lien, E. A. M. Klumperink, B. Tenbroek, J. Strange, and B. Nauta, "Enhanced-selectivity high-linearity low-noise mixer-first receiver with complex pole pair due to capacitive positive feedback," *IEEE J. Solid-State Circuits*, vol. 53, no. 5, pp. 1348–1360, May 2018.
[23] S. Krishnamurthy and A. M. Niknejad, "Design and analysis of enhanced mixer-first receivers achieving 40-dB/decade RF selectivity," *IEEE J. Solid-State Circuits*, vol. 55, no. 5, pp. 1165–1176, May 2020.

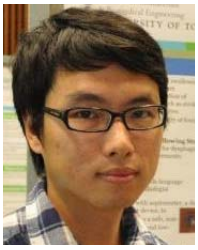

Shi Bu (Graduate Student Member, IEEE) received the B.Eng. and M.Phil. degrees in electronic engineering from The Chinese University of Hong Kong, Hong Kong, in 2014 and 2016, respectively. He is currently pursuing the Ph.D. degree in electrical and computer engineering with the University of California, Los Angeles, CA, USA.

His research interest includes analog, mixed-signal, and RF integrated circuits for communication and power-management applications.

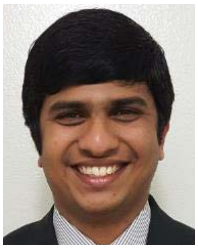

Sameed Hameed (Member, IEEE) received the B.Tech. degree in electrical engineering from IIT Madras, Chennai, India, in 2011, and the M.S. and Ph.D. degrees in electrical engineering from the University of California, Los Angeles (UCLA), CA, USA, in 2013 and 2017, respectively.

In 2013, he was an RFIC Design Intern at Broadcom, Irvine, CA, USA. Since 2016, he has been with Silvus Technologies, Inc., Los Angeles, where he is currently a Senior RFIC Engineer. His research is focused on agile RF receivers and baseband circuits.

Dr. Hameed was a recipient of the Electrical Engineering Department Fellowship in 2013 for placing first in the 2013 Ph.D. preliminary exam in circuits and embedded systems, the UCLA Graduate Division Fellowship in 2014, the Broadcom UCLA Fellowship during the 2015–2016 academic year, the Dissertation Year Fellowship and the MediaTek UCLA Fellowship during the 2016–2017 academic year, the IEEE Solid-State Circuits Society 2015–2016 Predoctoral Achievement Award, the 2016–2017 IEEE Solid-State Circuits Society Student Travel Grant, and the UCLA Electrical Engineering Department's 2016–2017 Distinguished Ph.D. Dissertation in Circuits and Embedded Systems Award. He has served as a Reviewer for the IEEE JOURNAL OF SOLID-STATE CIRCUITS, the IEEE TRANSACTIONS ON CIRCUITS AND SYSTEMS—I: REGULAR PAPERS, and the IEEE TRANSACTIONS ON CIRCUITS AND SYSTEMS—II: EXPRESS BRIEFS.

Sudhakar Pamarti (Senior Member, IEEE) received the B.Tech. degree in electronics and electrical communication engineering from IIT Kharagpur, Kharagpur, India, in 1995, and the M.S. and Ph.D. degrees in electrical engineering from the University of California, San Diego, CA, USA, in 1999 and 2003, respectively.

He has either worked for, or consulted with, both software and hardware companies, such as Hughes Software Systems, Rambus, SiTime, Texas Instruments, Alterra, and so on. He is currently a Professor of electrical and computer engineering at the University of California, Los Angeles, CA, USA. His research interests are in analog, mixed-signal, and RF integrated circuit design, specifically in developing signal processing techniques to overcome circuit impairments.

Dr. Pamarti was a recipient of the National Science Foundation's CAREER Award. He is an IEEE Solid-State Circuits Society Distinguished Lecturer and serves on the technical program committees of the IEEE Custom Integrated Circuits Conference and the IEEE International Solid-State Circuits Conference, and has, in the past, been a Guest or a Regular Associate Editor of the IEEE TRANSACTIONS ON CIRCUITS AND SYSTEMS—I: REGULAR PAPERS, the IEEE TRANSACTIONS ON CIRCUITS AND SYSTEMS—II: EXPRESS BRIEFS, and the IEEE JOURNAL OF SOLID-STATE CIRCUITS.